

Modeling and Simulation of Novel Semiconducting Metal Oxide Gas Sensors for Wearable Devices

Ayoub Lahlalia, Lado Filipovic, and Siegfried Selberherr

Abstract—Our work focuses on the design and rigorous evaluation of two novel designs for semiconducting metal oxide (SMO) gas sensors with different shapes and sizes, in order to assess the most efficient layout geometry in terms of power consumption, membrane stability, and temperature distribution. The aim of this paper is to provide two designs, one to be used for a thin sensing film and the other to be applied with a nanowires sensing layer. Both designs implement innovative aspects, allowing for an improvement in state-of-the-art sensors' selectivity and power consumption, which make the product suitable for use on a wide variety of applications. To further support the simulation results, an analytical model based on a Cauer network is presented for estimating the power consumption of the device. We demonstrate the ability of SMO sensors to operate at 300 °C with high uniform temperature over the sensing material and ultra-low power consumption of roughly 8 mW. In addition, a microheater array design is presented, which is able to heat two active sensing layers to 270 °C and 350 °C simultaneously in 40 μ s. Both designs are analyzed for stability, and it was found that the stress generated in the membranes and the resulting deformation is minimal, improving the device stability and reliability.

Index Terms—Gas sensor, microheater array, low power, semiconducting metal oxide, electro-thermal simulation.

I. INTRODUCTION

THE semiconducting metal oxide (SMO) gas sensor is on its way to becoming the world's universal MEMS sensor, since, it can be used in many emerging applications such as sensor networks, RFID tags, medical applications, food quality monitoring, wearable devices, etc [1], [2]. Furthermore, according to the world health organization more than 7 million people die each year as a result of exposure to air pollution [3], which prompted scientists to search for a new technology, viable and scalable, for monitoring air quality in order to save lives and make people aware, how vulnerable they are to the impacts of climate change. The SMO gas sensor is a good candidate, when compared to other sensors available on the market, as it can be used in many applications thanks to its small footprint, high sensitivity, and fast response; nevertheless, a further reduction in power consumption and improved selectivity are still necessary in order to enable wide marketability of this innovative device. Nowadays, the lowest power consumption in commercialized SMO gas

sensors is higher than 15mW when operated continuously at 300°C [4]–[6]. The gas sensor which was nominated as a finalist in the The 2017 Annual Creativity in Electronics (ACE) Awards (CCS811) has a power consumption of 46mW [7]. Nevertheless, it is considered and intended for portable applications.

The operating principle of the SMO gas sensor relies on heating the sensing layer to a temperature between 250°C and 550°C using the joule effect. The operating temperature required is dependent on the sensing material used and the type of targeted gases. In order to promote the adsorption and electron exchange between the gas and the sensing layer, the sensor must operate at high temperatures in the presence of an oxygen-rich ambient [8], [9]. During the last few years, there has been extensive research on gas sensors working at room-temperature. Gas sensors based on nanostructured materials were found to be promising among the sensor family, as they are characterized by high sensitivity and a fast response. However, recovery time is still a major issue preventing the use of this technology for consumer applications, which is very important for high accuracy measurements in real time. In addition, the irreversibility of the sensor response and poor selectivity dramatically impact the device reliability and performance [10]. So far, there are attempts to overcome this using a Carbon Nano Tubes based gas sensor as a trigger for the SMO gas sensor [11].

For decades, metal oxides have been the most widely used materials for gas detection due to their ability to react with dioxygen [12]. Among the most commonly used in the commercial market are tin dioxide (SnO_2), zinc oxide (ZnO), and tungsten trioxide (WO_3), since they fulfil all the requirements for a good gas sensing performance [13]–[15], compared to others, such as In_2O_3 , ITO, CdO , ZnSnO_4 , Nb_2O_5 etc [16]–[18]. These materials can be deposited on top of a suspended membrane using a variety of techniques and in different forms such as thin film, nanocompound, nanobelt, and nanowires.

Although thin film metal oxides have significant application potential, they can be degraded due to many factors. For instance, a quick change in the sensor operating temperature leads to the formation of many cracks in the thin film surface. Therefore, using heat pulsing mode damages the sensor within only a few hours of operation, since the sensing layer resistance changes as a result of transformation in the thin film structure [19], [20]. To overcome this limitation, we propose a novel sensor design dedicated to the thin film sensing layer, which can meet essential needs such as a uniform thermal

Manuscript received December 4, 2017; accepted December 27, 2017. Date of publication January 5, 2018; date of current version January 31, 2018. The associate editor coordinating the review of this paper and approving it for publication was Prof. Ravinder S. Dahiya. (Corresponding author: Ayoub Lahlalia.)

The authors are with the Department of Microelectronics, Institute for Microelectronics, Technische Universität Wien, 1040 Wien, Austria (e-mail: lahlalia@iue.tuwien.ac.at).

Digital Object Identifier 10.1109/JSEN.2018.2790001

distribution, ultra low power consumption, high selectivity, electrodes definition, and low membrane deformation; note that the latter two are quite often neglected in published studies.

More recently, nanowires, nanocompounds, and nanobelts attracted attention from researchers thanks to their high sensitivity, selectivity, and reliability compared to thin films. It has been demonstrated that SnO₂ nanowires have the ability to detect harmful gases such as volatile organic compounds at rates 30 times higher than the SnO₂ thin film [21]. Moreover, the nanowires sensing layer shows diverse responses towards different gases, providing additional methods to distinguish between each individual gas. This feature sparked the interest of many electronic nose developers and can be employed along with a simple electronic circuit for its signal processing [21], [22]. Despite all these benefits, SnO₂ nanowires have an anomalous response towards specific gases such as SO₂ and H₂S, which can dramatically influence the sensor response. For instance, reducing gas becomes an oxidizing gas at a specific temperature and in rare cases the target species could degrade the sensitivity of the sensor [21], [23], [24].

In this manuscript two sensors with different shapes and sizes are proposed to match various sensor designers' needs. For this purpose, the designs have been modeled using different structures in order to improve the membrane stability, power consumption, and temperature uniformity in the active area. These features are a crucial requirement for portable applications such as wearable athletic clothing, smart watches, and smart rings [25]. The sensors are rigorously analyzed using finite element simulations using COMSOL Multiphysics [26]. The achievements obtained with the proposed designs are discussed in the sections which follow.

II. GAS SENSOR DESIGNS

The SMO gas sensor designs covered in this work implement several innovative details, which meet different sensor designers' needs while easing the fabrication process requirements and improving sensor properties such as power consumption and thermal insulation - two essential factors for a monolithic integration of the sensor with associated electronics. Each device has an area of 0.9mm × 0.6mm with a structural membrane stack formed by a 500nm thick silicon dioxide (SiO₂) layer, a 300nm thick silicon nitride (Si₃N₄) layer, and another 500nm thick silicon dioxide layer. Platinum was chosen for the microheater and electrodes material for its stability, linearity, and resistance to oxidation at a broad range of operating temperatures. AlCu was chosen instead of gold for the microheater pads due to its higher electrical conductivity and lower thermal conductivity. To ensure electrical insulation between the microheater and sensing layer electrodes a 300nm thick silicon dioxide layer is deposited on top of the microheater.

The reaction between the gas and the thin sensitive compact film occurs only on the surface, as depicted in Fig. 1 [27]. For this reason it is better to use electrode strips on top of the thin sensitive layer instead of interdigitated combs (a structure rich in meanders and cavities), leading to improved gas sensor sensitivity, while reducing the likelihood of crack formation

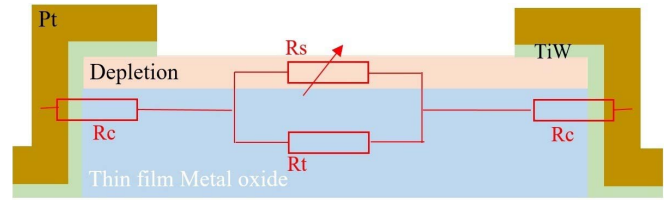


Fig. 1. Cross section of a thin film sensing layer. R_s is the depletion region resistance; R_t and R_c are the bulk resistance and the contact resistance, respectively.

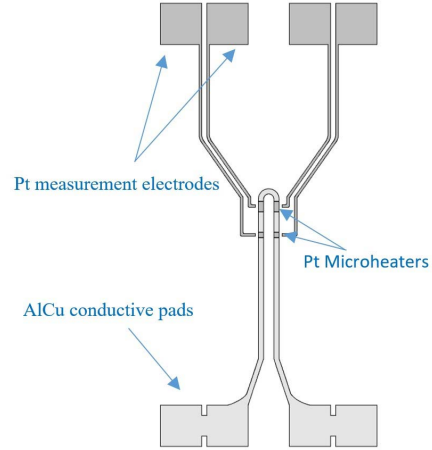


Fig. 2. Design of the microheater array and measurement electrodes.

on the surface of the sensing layer [28]. This feature is highly recommended for monitoring air quality, since a detection of gases in trace concentrations down to few ppb is required to detect any change in the surrounding air quality. The only drawback of using this shape is the risk of rapidly saturating harmful gas detection at only a few ppm. In order to form Ohmic contacts and to avoid the appearance of a junction between electrodes and the sensitive layer, a 25nm layer of Titanium Tungsten (TiW) is stacked between the sensing layer and the metal contact. The sensitivity response S_{gas} of the gas sensor is defined by how much the resistance changes in the presence of a target gas, when compared to the resistance in the baseline ambient:

$$S_{gas} = \frac{R_{air} - R_{gas}}{R_{air}} \quad (1)$$

R_{air} represents the baseline resistance after stabilization in ambient air and R_{gas} is the electrical resistance of the sensitive layer after the introduction of a reacting gas in the ambient.

A. Microheater Array Design

The microheater array design is a combination of small resistances placed in an array instead of a conventional microheater (Fig. 2), used for heating the sensing layer at different locations and at different temperatures. This allows for an improvement in the desired temperature distribution over the sensitive material while reducing the power consumption. In addition, small resistances allow for an ultra fast thermal response time, which enables the microheater to operate in an ultra-short pulsing mode, thus reducing the average power consumption to a few hundred μW .

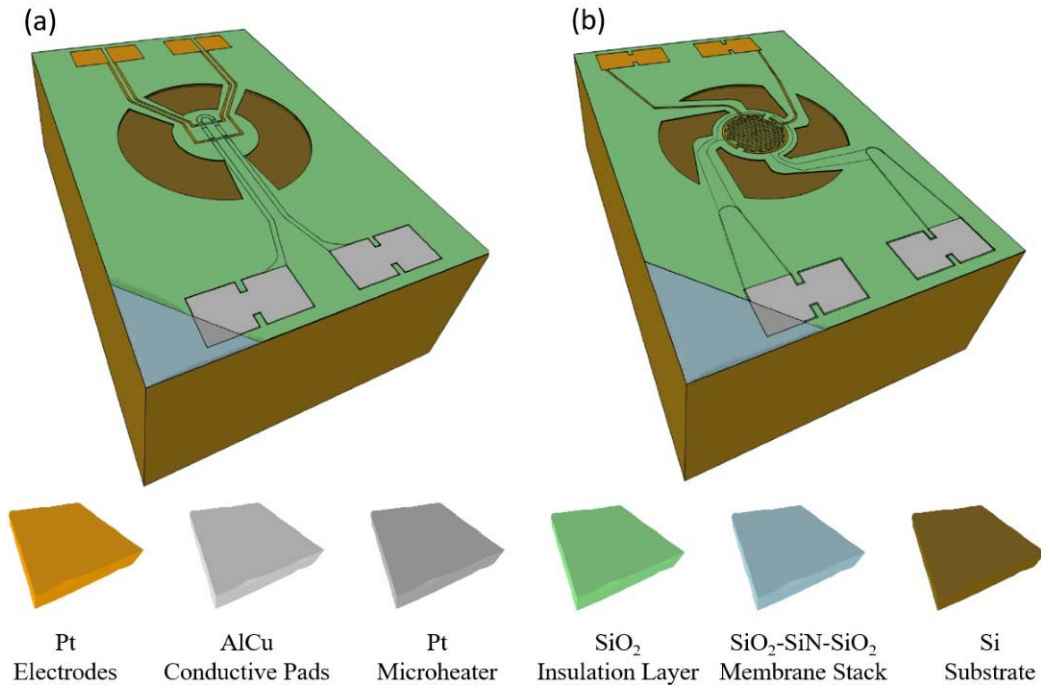


Fig. 3. Structure of the SMO gas sensors. (a) Microheater array design. (b) Dual-hotplate design.

The locations of the small heaters have been optimized in such a way that the active area operates at a high temperature uniformity, with variation within 10°C . This feature has been used to improve the selectivity of the thin film metal oxide by gathering multiple sensing layers in the same membrane structure, as already reported in the work of Victor V. Sysoev *et al.* [29]. Since the sensitivity of thin metal oxide films towards gases depends on the operating temperature [9], each sensing layer is heated to a specific temperature, which remains uniform over the desired sections. Measured data can subsequently be treated using non-parametric analysis, such as principal component analysis (PCA), discriminant function analysis (DA), and neural Networks (RN) in order to distinguish between each gas, thus improving the selectivity of the thin film SMO gas sensor [12], [30], [31]. We present novel design with two sensing layers, deposited in the same membrane structure in Fig. 3a. By adjusting the dimensions and location of each microheater the sensor can easily be modified to accommodate more than two sensitive materials.

Fig. 4 shows the sensitivity of doped and undoped SnO_2 thin film towards methane, hydrogen, carbon monoxide, and propane at different working temperatures. As can be seen from the graph the operating temperature defines the selectivity of the sensor; therefore, this microheater array design solves one of the major problems related to the selectivity of thin film SMO gas sensors.

A slope of 45 degrees is added to the end of each microheater contact in order to reduce the current density accumulation between metallization lines, which allows to further decrease the electrical losses and avoid breaking connection lines.

Fig. 5 shows the current density in metallization lines over the microheater for designs with and without slopes added

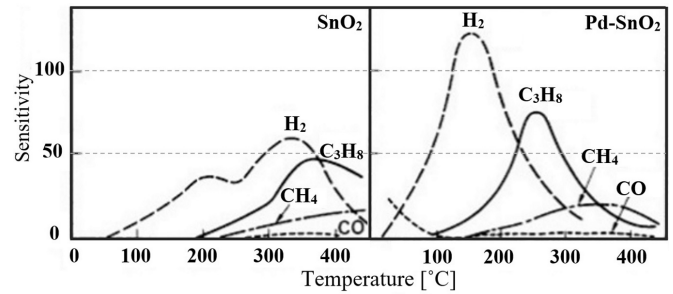


Fig. 4. Sensitivity of doped and undoped SnO_2 thin film layer as a function of operating temperature towards different gases. The concentrations of gases in air are 0.5% CH_4 , 0.8% H_2 , 0.02% CO , 0.2% C_3H_8 [32].

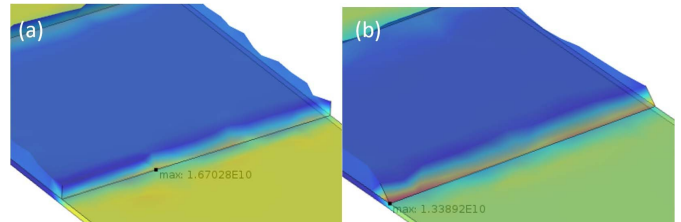


Fig. 5. Maximum current density in metallization lines (a) without slope and (b) with slope.

to the end of the AlCu lines. The maximum current density measured in conventional design is about $16.7 \times 10^9 \text{ A/m}^2$, while the novel design has only $13.4 \times 10^9 \text{ A/m}^2$; a reduction of about 20%. Therefore, using slopes between connection lines leads to an improved sensors efficiency.

B. Dual-Hotplate Design

The dual-hotplate sensor shown in Fig. 3b is a novel design which uses a single circular microheater, as presented in the work of Elmi *et al.* [33], along with two passive

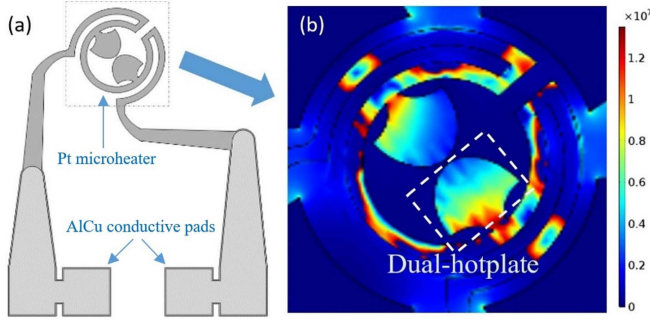


Fig. 6. (a) Microheater structure of the dual-hotplate design. (b) Heat flux (W/mm^2) through the microheater, dual-hotplate, and membrane sensor at 300°C .

micro-hotplates. These were used for the purpose of improving the temperature distribution over the sensing layer, while keeping the power consumption at a minimum, which is a critical point for stability of the baseline. A small variation in temperature over the sensing layer leads to baseline drift, thereby creating a change in the resistivity of the sensitive material. In addition, working at a heterogeneous temperature activates more interactions between gases and sensitive layer, which influences the selectivity and stability of the sensor. The operating principle of this novel structure relies on the high thermal conductivity of platinum compared to silicon dioxide and silicon nitride, which means that the heat flux through the Pt dual-hotplate is greater than the heat flux through the membrane. By optimizing the position of these two metal plates, as shown in Fig. 6, the uniformity of the temperature can be improved.

A new membrane shape has been used as part of the dual-hotplate design formed by four curved micro-bridges in order to provide better insulation against heat losses from the heater to the substrate. This results in a minimization of the heat dissipation and a reduction of the power consumption down to a few mW. To ensure the mechanical and thermal stability of the membrane sensor before proceeding with the fabrication step, electro-thermal-mechanical simulations have been performed on the novel structures and the results are shown and discussed in Section 4.

III. DEVICE SIMULATION

A. Simulation Parameters

The sensors were designed with a modeling tool and the electro-thermal-mechanical simulations were subsequently performed in a finite element environment. Simulation parameters are required for the various materials for the membrane; where silicon dioxide and silicon nitride have been chosen in this study due to their high mechanical stability and low thermal and electrical conductivity. The boundary conditions were initially set to 20°C for ambient temperature and material temperature, whereas the temperature coefficient of resistance of platinum and the temperature of the substrate bottom were fixed at $3730\text{ppm}/^\circ\text{C}$ and 20°C , respectively [34].

Regarding the heat transfer coefficient, which is a quantitative characteristic of convective heat transfer between the air and sensor surfaces, an empirical value was used for its

calculation, describing the heat transfer due to fluid motion and conduction through the air. For simplification, the heated membrane area is considered as a horizontal plate of characteristic size l . Therefore, the mean heat transfer coefficient h_m can be calculated as follows:

$$h_m = \frac{Nu \cdot k(T_m)}{l} \quad (2)$$

where $k(T_m)$ is the thermal conductivity at $T_m = (T_{hot} + T_a)/2$, T_a is the ambient temperature, and Nu is the Nusselt number, calculated on the assumption of laminar flow, in which:

$$Ra \cdot f_2(Pr) < 7 \times 10^4 \quad \text{and} \quad 0 \leq Pr \leq \infty \quad (3)$$

given by

$$Nu_m = 0.766(Ra \cdot f_2(Pr))^{1/5} \quad (4)$$

with

$$Ra = \frac{\beta_\infty(T_{hot} - T_a)g \cdot l^3}{v^2} Pr \quad (5)$$

$$f_1(Pr) = \frac{\beta_\infty}{v^2} Pr \cdot f_2(Pr) \quad (6)$$

$$f_2(Pr) = [1 + (\frac{0.322}{Pr})^{11/20}]^{-20/11} \quad (7)$$

where Ra and Pr are the Rayleigh and Prandtl numbers, respectively, β_∞ is the thermal expansion coefficient, v is the kinematic viscosity, and g is the acceleration due to gravity.

In order to calculate the mean heat transfer coefficient as a function of the temperature for our designs, the $f_1(Pr)$ function has been used, which extracts the two unknown parameters from experiment, given in the work of Simon *et al.* [27], namely, Prandtl numbers and kinematic viscosity. Therefore, the new equation of the mean heat transfer coefficient can be expressed as:

$$h_m = \frac{k(T_m)}{l} 0.766(f_1(Pr) \cdot (T_{hot} - T_a) \cdot g \cdot l^3)^{1/5} \quad (8)$$

Further explanations and detailed calculations can be found in [35]. Another aspect dealing with heat conduction through air is taken into consideration, namely, the fact that the thermal conductivity of air changes as a function of the temperature. In this study, the numerical values used for the calculation of $k(T_m)$ are taken from [27], $k(293\text{K}) = 0.026\text{W K}^{-1}\text{m}^{-1}$ and $k(593\text{K}) = 0.044\text{W K}^{-1}\text{m}^{-1}$.

The influence of the temperature above the circular hotplate on the heat transfer coefficient is shown in Fig. 7. As expected, the coefficient is larger when the temperature increases, thereby increasing the power consumption. It should, however, be noted that the diameter of the circular membrane of $180\mu\text{m}$ is considered as the characteristic size of the horizontal plate, in addition, the loss of heat towards the substrate is neglected and the heat transfer coefficient of the membrane bottom is assumed similar to the top face of the micro-hotplate.

The heat losses through radiation were considered to be negligible compared to heat losses by conduction and convection, which are the principal causes of heat dissipation in a conventional SMO gas sensor [36]. In other words, the heat loss mechanism is produced by heat conduction through the air

TABLE I
PARAMETERS FOR A THERMAL EQUIVALENT ELECTRICAL CIRCUIT MODEL

Thermal parameter	Electrical equivalent	Thermal parameter	Electrical equivalent
Temperature $T(K)$	Voltage $V(V)$	Heat flow $P(W)$	Current $I(A)$
Specific heat $C_p(J/Kg.K)$	Permittivity $\epsilon(F/m)$	Thermal conductivity $k(W/K.m)$	Electric conductivity $\sigma(S/m)$
Thermal resistivity $\rho_{th}(K.m/W)$	Electric resistivity $\rho_{el}(\Omega.m)$	Heat $Q(J = W.s)$	Charge $Q(C = A.s)$
Resistance $R_{th}(K/W)$	Resistance $R(\Omega = V/A)$	Capacitance $C_{th}(J/K)$	Capacitance $C(F)$

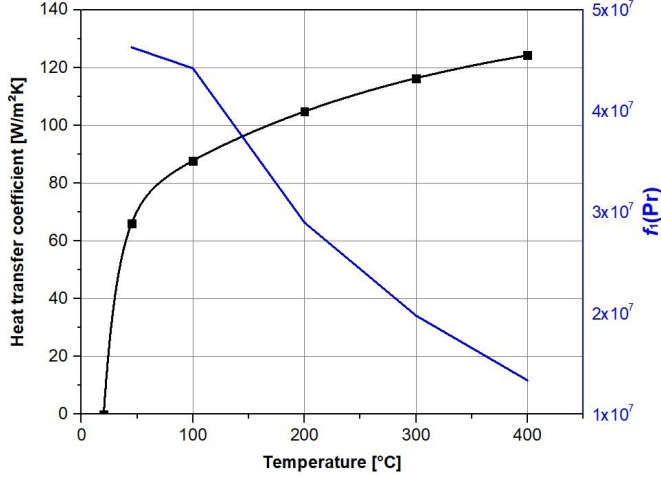


Fig. 7. Heat transfer coefficient for free convection above the micro-hotplate with characteristic size of $180\mu m$, and numerical values of function $f_1(Pr)$ as a function of the temperature of the heated membrane area.

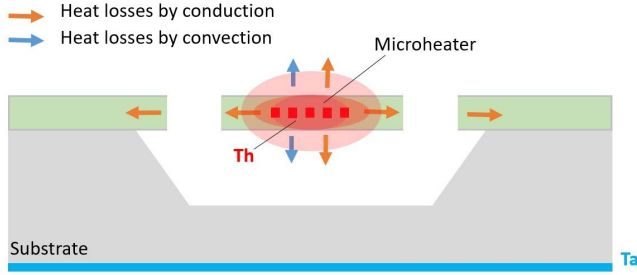


Fig. 8. Heat loss mechanisms through the SMO gas sensor. T_h is the temperature of the microheater; T_a is the ambient temperature.

and from the microheater to the substrate through metallization lines and micro bridges of the membrane, while heat convection is caused by the interaction between the sensor surface and the surrounding air, as depicted in Fig. 8. In fact, choices in the sensor design such as the membrane and microheater structure and choice of material play a major role in defining the sensor performance.

B. Heat Transfer Model

A simple Cauer network model was used in this study with the purpose of calculating the temperature generated by the microheater as a function of the power consumption. As mentioned earlier, the electric power applied to the heater is dissipated mainly by two mechanisms: heat conduction and heat convection. These can be calculated using three important parameters relating material properties, as thermal

resistance R_{th} , thermal capacitance C_{th} , and convection resistance R_{conv} .

$$R_{th} = \frac{t}{k \cdot A} \quad (9)$$

$$C_{th} = c_e \cdot \rho \cdot V \quad (10)$$

$$R_{conv} = \frac{1}{h_m \cdot S_r} \quad (11)$$

t is the thickness of the layer perpendicular to the heat flux; k is the thermal conductivity; A is the cross-sectional area perpendicular to the heat flow; c_e is the specific heat; ρ is the material density; h_m is the heat transfer coefficient of the material and S_r is the exposed area from which the heat flows.

The electro-thermal simulation of the gas sensor is based on dividing the entire sensor into small cuboids, noting that their sizes depend on the mesh used. Each individual piece is modeled by a thermal resistance in parallel with a thermal capacitance, except for the microheater, which is represented by a heat source and all surfaces in contact with air are represented by convection resistances. It should be noted that each thermal parameter can be modeled by an electrical equivalent, where each thermal propriety is mapped by an equivalent electrical behaviour. For instance, the temperature is equivalent to voltage and heat flow is analogous to current as shown in Table 1. Therefore, the electrical parameter can be added to the heat transfer equation (12), allowing for the calculation of the electric power consumption as a function of the heater temperature:

$$\rho \cdot c_e \cdot \frac{\partial T}{\partial t} = \nabla(k \cdot \nabla T) + Q_e \quad (12)$$

where T is the temperature in K, and Q_e represents joule heating of the microheater in Watt. Knowing that $Q_e = J \cdot E$ (12) can be expressed as:

$$\rho \cdot c_e \cdot \frac{\partial T}{\partial t} = \nabla(k \cdot \nabla T) + J \cdot E \quad (13)$$

given that:

$$J = \sigma E + J_e \quad (14)$$

and

$$E = -\nabla V \quad (15)$$

where J is the current density in A/m^2 , E is the electric field in V/m , J_e is the external current density (in this case equal to 0), and σ is the electrical conductivity in S/m , which can be described by the following expression:

$$\sigma = \frac{1}{\varrho_a(1 + \alpha(T - T_a))} \quad (16)$$

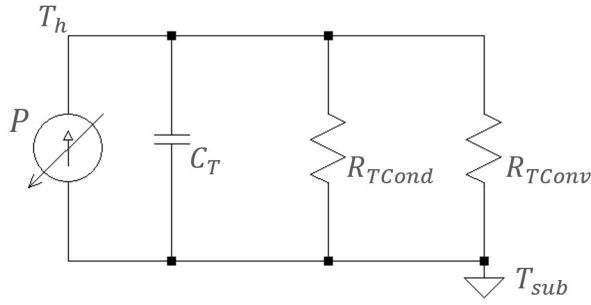


Fig. 9. Equivalent electric circuit of electro-thermal behavior of the sensor.

where q_a is the electrical resistivity at temperature T_a . By substituting (14) and (15) into (13), we obtain:

$$\rho \cdot c_e \frac{\partial T}{\partial t} = \nabla(k \cdot \nabla T) + \sigma \cdot \nabla V \cdot \nabla V \quad (17)$$

The left hand side of the heat transfer equation (17) can be modeled with a thermal capacitance, found by integrating the time dependent term [37]

$$\rho \cdot c_e \frac{\partial}{\partial t} \int_V T dV \quad (18)$$

Rewriting (17) after integration we obtain:

$$C_{th} \frac{\partial T}{\partial t} = \frac{-\Delta T}{R_{th}} + R(T) \cdot I^2 \quad (19)$$

where $\Delta T = (T_{hot} - T_a)$.

Since the heat flux generated by the micro-heater has an opposite direction to the heat flux coming from the bottom of the sensor, which represents the flow of air at room temperature, a negative sign is added to the first term on the right hand side of (19). Therefore, this can be modeled by an equivalent electrical circuit shown in Fig. 9.

where P represents the heat flux, R_{TCond} and R_{TConv} are the overall thermal and the convection resistances of the entire sensor, respectively, and C_T is the thermal capacitance of the sensor. If we consider the steady state condition of the model, the term on the left hand side of equation (19) must be equal to zero; therefore, the heat transfer equation can be expressed as:

$$P = \frac{\Delta T}{R_{th}} = \Delta T \left(\frac{1}{R_{TCond}} + \frac{1}{R_{TConv}} \right) \quad (20)$$

For clarity and to avoid increasing the model complexity, an example of a Cauer network model is presented in the section below showing the steps of modeling the membrane structure. However, instead of modeling the entire sensor, this study focuses solely on the membrane which is responsible for the bulk of the power consumption. To confirm the analytical model, the power consumption of the entire sensor without the sensitive layer and the accompanying electrodes is compared with the analytical results.

To analyze the thermal behavior and estimate the power consumption of the membrane stack in steady state, each insulation layer is divided into small bricks as shown in Fig. 10a and modeled by thermal resistances, expressed in terms of thermal conductivity. Fig. 10b shows the heat loss by convection modeled by R_{PConv} , which represents the convection

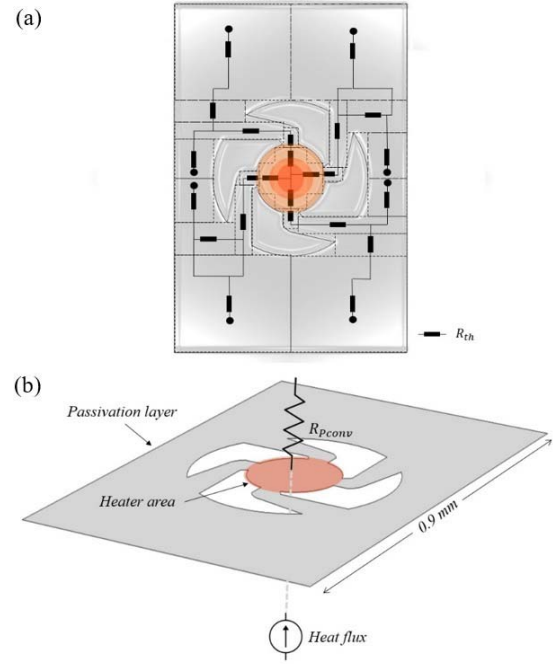


Fig. 10. Model to consider heat loss of the passivation layer (a) by conduction and (b) by convection.

resistance of the top passivation layer. The thickness, length, and width of the passivation layer are $0.5\mu\text{m}$, 0.9mm , and 0.6mm , respectively, while the circular membrane has a radius of $90\mu\text{m}$. In order to analyse the circuit equivalent, LTspice, a circuit analysis software [38], was used to calculate the power dissipated through the membrane. It should be noted that different assumptions were taken into account in order to match real-world conditions, meanwhile simplifying the electro-thermal model: the circular suspended diaphragm is heated at a uniform temperature of 300°C , vertical heat loss is neglected since the layers are very thin, the substrate is thermally isolated from the heated membrane, the depth of the cavity is sufficient for preventing temperature diffusion to the substrate, electrical losses between layers are negligible, and the average temperature in each beam is $(T_{hot} + T_a)/2 = 160^\circ\text{C}$ when the microheater reaches a temperature of 300°C . It is necessary to state that the model is useful only for specific designs which match the assumptions mentioned above; therefore, the power consumption of the microheater array design, described in Section 2.1, cannot be calculated in the same way.

Using (9)-(11), with dimensions shown in Fig. 11a, the numerical value of the thermal and convection resistances can be calculated as follows:

$$R_{SiO_2.x} = \frac{70\mu\text{m}}{1.4 \cdot (0.5\mu\text{m} \cdot 40\mu\text{m})} = 2.5 \times 10^6 \text{ K/W} \quad (21)$$

$$R_{SiO_2-x} = \frac{130\mu\text{m}}{1.4 \cdot (0.5\mu\text{m} \cdot 60\mu\text{m})} = 3.0 \times 10^6 \text{ K/W} \quad (22)$$

$$R_{SiN.x} = \frac{70\mu\text{m}}{20 \cdot (0.3\mu\text{m} \cdot 40\mu\text{m})} = 0.2 \times 10^6 \text{ K/W} \quad (23)$$

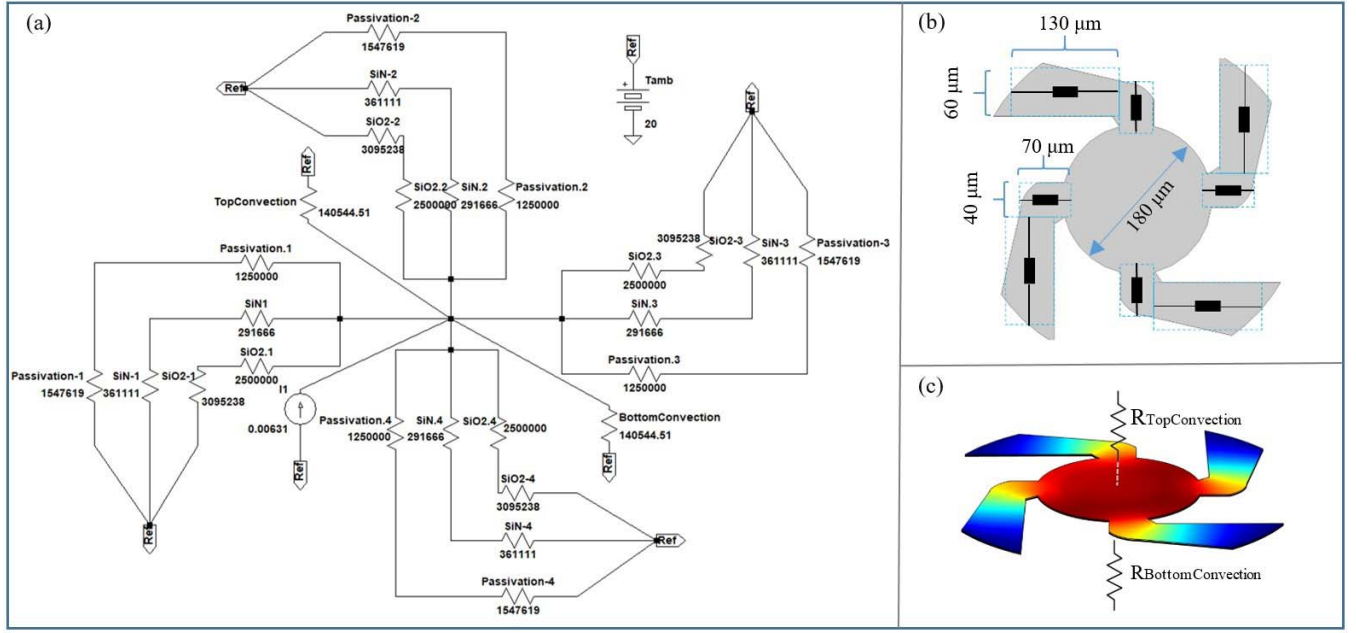


Fig. 11. (a) Electro-thermal model of the dual-hotplate design with (b) the dimensions of the membrane structure and (c) the heat loss in membrane by convection.

$$R_{SiN-x} = \frac{130\mu m}{20 \cdot (0.3\mu m \cdot 60\mu m)} = 0.3 \times 10^6 K/W \quad (24)$$

$$R_{Passiv-x} = \frac{70\mu m}{1.4 \cdot (1\mu m \cdot 40\mu m)} = 1.2 \times 10^6 K/W \quad (25)$$

$$R_{Passiv-x} = \frac{130\mu m}{1.4 \cdot (1\mu m \cdot 60\mu m)} = 1.5 \times 10^6 K/W \quad (26)$$

$$R_{TC} = R_{BC} = \frac{1}{(116.32 \cdot \pi \cdot (90\mu m)^2) + (4 \cdot 98 \cdot S_b)} = 0.14 \times 10^6 K/W \quad (27)$$

where R_{SiO_2-x} and R_{SiN-x} are the thermal resistances of the bottom silicon dioxide layer of the beam, R_{SiN-x} and R_{SiN-x} are the thermal resistances of the silicon nitride layer of the beam, $R_{Passiv-x}$ and $R_{passiv-x}$ are the thermal resistances of the top silicon dioxide layer and passivation layer of the beam, R_{TC} and R_{BC} are the convection resistances of the top and bottom surface of the membrane, respectively, and S_b is the top surface area of the beam. For the calculation of the convection resistance, the heat transfer coefficient at 160°C and 300°C was extracted from Fig. 7, resulting in values of 98W/m²K and 116W/m²K, respectively.

Fig. 11 shows the electro-thermal model equivalent of the membrane, where an extra 20V DC source at room temperature, considered as a reference, is introduced to the circuit. In order to reach 300V, which is equivalent to 300°C, 6.3mA was applied to the electrical circuit by a current generator. This results in a good agreement with simulation results of the entire sensor without a sensing layer and the accompanying measurement electrodes, which requires 6.8mW for the same temperature. In order to understand the difference between finite element simulations and our analytical model, a comparative simulation was performed at several input powers. The resulting microheater temperature is

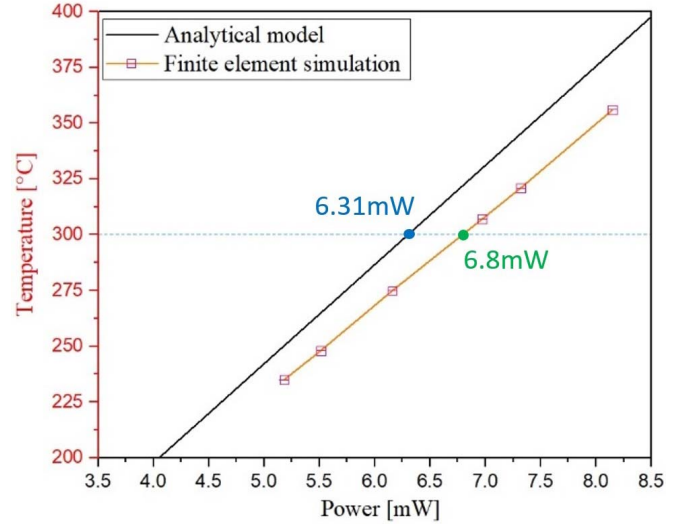


Fig. 12. Temperature as a function of applied power to the heater of dual-hotplate design.

shown in Fig. 12. To properly estimate the thermal response of the microheater, a thermal capacitance of the circular membrane must be taken into account in the electro-thermal circuit equivalent.

IV. DISCUSSION

The electro-thermal-mechanical simulations were performed using COMSOL Multiphysics [26], which is based on the finite element method (FEM). Silicon dioxide and silicon nitride are used for the membrane. The material properties are summarized in Table 2. Simulations were carried out in steady state and transient state for the entire sensor, including the 0.5μm thin SnO₂ film. Note that due to the complexity of

TABLE II
MATERIAL PROPERTIES USED IN THE SIMULATIONS

Material	Thermal conductivity (W m ⁻¹ K ⁻¹)	Thermal capacity (J Kg ⁻¹ K ⁻¹)	Intrinsic stress (GPa)	Density (Kg m ⁻³)	Coefficient of thermal expansion (10 ⁻⁶ × K ⁻¹)
Si	150	700	—	2329	—
SiO ₂ , GTO/ LPCVD	1.4	730	-0.235[39]/ -0.07 [39]	2200	0.5
Si ₃ N ₄ , PECVD	20	700	0.37 [39]	3100	2.3
Pt	71.6	133	—	31450	8.8
AlCu	240	915	—	2700	9
SnO ₂	64	1000	—	6950	—

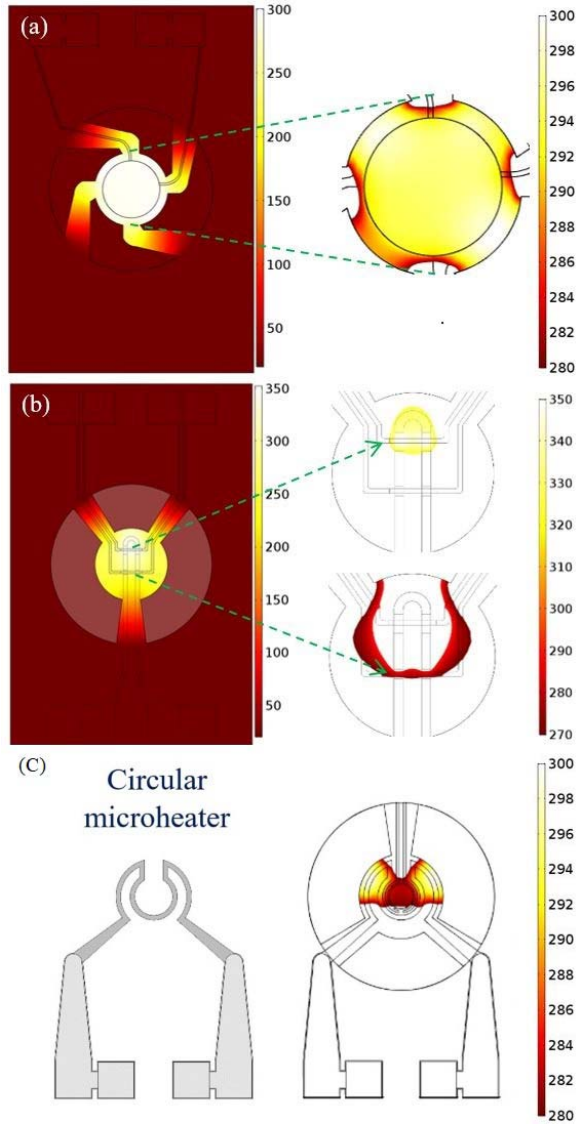


Fig. 13. Simulation of the thermal distribution (°C): (a) in dual-hotplate design, (b) in microheater array design, and (c) in circular microheater.

modeling sensitive nanowires, a thin film layer is used for the dual-hotplate design.

A. Electro-Thermal Simulations

Fig. 13a shows the temperature distribution over the circular membrane for the dual-hotplate design, where a high uniformity in temperature distribution over the active sensitive region can be observed, unlike the case of the design with

only a circular microheater (Fig. 13c). The curved microbridges show a good thermal insulation from the heated area to the substrate, which leads to a minimization in the power consumption. In order to reach the target temperature of 300°C, the platinum microheater consumes 7.3mW power in continuous mode, whereas the transient simulations show that the sensitive layer can be heated to a uniform temperature of 300°C within 20ms. Concerning the microheater array design, a highly uniform temperature over each sensitive layer is obtained, as can be seen in Fig. 13b. The required power consumption by the heaters in order to reach 350°C over the first sensitive material and 270°C over the second one is 9.31mW. Each sensitive layer operates at different temperature with the aim of improving the selectivity of the thin film sensing layer. The microheater array requires less than 40μs to heat the sensitive materials from room temperature up to 350°C.

To design a good microheater and to avoid thermal cracking of the sensor, the power consumption and temperature gradient must be as low as possible. The dimensionless Biot number (Bi) was used to determine whether or not the membrane will withstand the physical strain at high temperature [40]. It is defined as the value obtained when dividing the surface heat coefficient by the membrane heat conductivity, as shown below:

$$Bi = \frac{h_m \cdot L}{k_T} \quad (28)$$

$$L = \frac{V}{A} \quad (29)$$

$$k_T = \sum_{i=1}^n k_i \cdot t_i / \sum_{i=1}^n t_i \quad (30)$$

L , V and A are the characteristic length, volume, and surface area of the entire membrane, respectively. k_T is the thermal conductivity of the membrane stack. The Biot number for both sensors presented here is below 0.1, which means that the heat convection from the membrane surface is much slower than the heat conduction inside of it, and the temperature gradient inside the membrane is insignificant [40]. Fig. 14 shows that the maximum temperature gradient is located at the edges of the membrane beams and the microheater in both designs. Note that a maximum temperature gradient near the measurement electrodes has been observed only for the microheater array design, which may lead to eventual electromigration failure [41], thus influencing the gas sensor response and lifetime.

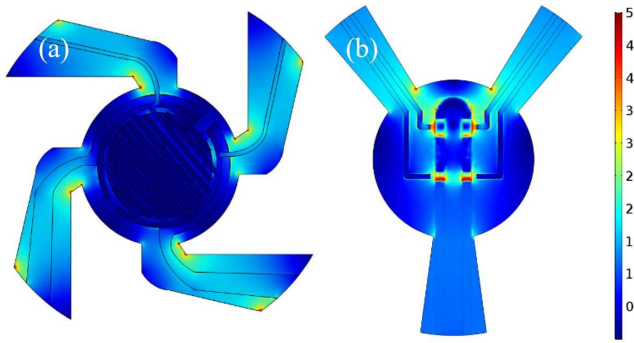


Fig. 14. Temperature gradient ($^{\circ}\text{C}/\mu\text{m}$): (a) in dual-hotplate design and (b) in microheater array design.

B. Mechanical Simulations

Until now, most studies dedicated to SMO gas sensor research are focused solely on the sensitive layer and the electro-thermal behavior of the micro-hotplate, neglecting the mechanical issues of the membrane structure. The internal stress accumulated during the fabrication stage is a major concern related to the MEMS sensor based micro-hotplate, which affects the performance of the device as well as its reliability. Furthermore, the thermal stress, introduced on top of the residual stress during operation caused by the difference in the thermal expansion coefficients between materials which compose the membrane structure, leads to a considerable increase in membrane deformation [42]. For this purpose, the average stress and deformation of the stacked thin film membrane ($\text{SiO}_2/\text{Si}_3\text{N}_4/\text{SiO}_2/\text{SiO}_2$) are evaluated in this study at different operating temperatures. Since the intrinsic stress for dielectric layers is dependent on the deposition technique used, it should be noted that the first layer of silicon dioxide is grown by thermally grown oxide at a temperature of 1100°C , the silicon nitride is deposited using plasma-enhanced chemical vapor deposition (PECVD) at 380°C , and the last two layers of silicon dioxide are deposited using low pressure chemical vapor deposition (LPCVD) at 420°C . As shown in Table 2, silicon dioxide experiences a compressive intrinsic stress, whereas the intrinsic stress in the silicon nitride is tensile. Therefore, for stress compensation, the silicon nitride layer is stacked between two silicon dioxide layers, knowing that, by adjusting the thickness of each layer, the average stress on the membrane stack σ_r can be minimized to an acceptable level: $-0.1\text{GPa} < \sigma_r < 0.1\text{GPa}$ [43].

Fig. 15 shows the average stress in both designs presented in the previous sections as a function of the microheater temperature. The maximum tensile stress generated during operation is lower than 0.2GPa for both designs, which means the membranes are not considerably stressed [43]. This is essential for complex sensor structures, since the presence of layers with high intrinsic stresses may lead to adherence problem [43] or to membrane instability and even collapse. The evolution of residual stresses depends on the membrane composition as well as its structure. As can be seen in Fig. 15, the deformation has a linear dependence on the microheater temperature. In addition, the direction of the membrane deformation is not affected by the effect of the heater metallization lines.

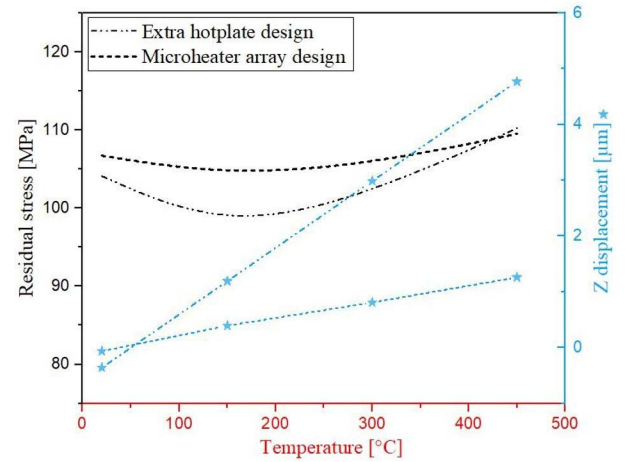


Fig. 15. The average residual stress and displacement of the membrane stack at different operating temperature.

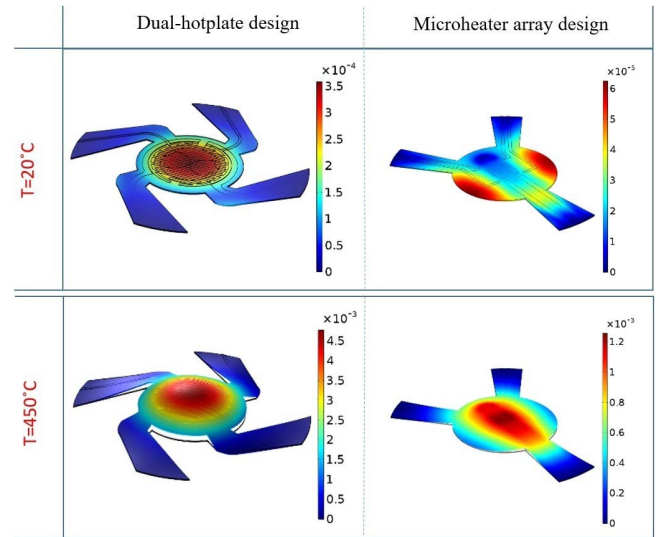


Fig. 16. Total displacement (mm) of the membrane stack at different operation temperatures.

Fig. 16 shows the vertical displacement of the membrane stack during operation at different temperatures. The dual-hotplate and microheater array designs have a maximum displacement of $5.12\mu\text{m}$ and $1.26\mu\text{m}$, respectively, when the membrane is heated from 20°C up to 450°C . This means that the thin film sensitive layer is less affected by the membrane displacement each time it is heated, which leads to a reduced likelihood of crack formation on the surface of the sensing material, thus stabilizing the baseline.

V. CONCLUSION

We have proposed two novel semiconducting metal oxide gas sensor designs which implement several innovative aspects in order to further decrease the overall power consumption, while improving the thermal behaviour and membrane displacement of the device during operation. The first sensor design gathers multiple sensitive layers on the same membrane structure, allowing to improve the sensing capability as well as to reduce the fabrication time and cost. The second sensor

design ensures a highly uniform temperature distribution over a nanowires sensing layer, while preventing thermal leaks from the heated circular membrane to the substrate. This keeps the power consumption at a minimum, which is roughly 8mW, when the microheater is heated at 300°C. To further support the rigorous simulations, we have presented an analytical model in calculating the temperature performance of the sensor when a current source is powering the Pt heater, which has demonstrated to be suitable and precise enough to be used as a tool kit for microheater developers. Our results also show a very low deformation of the membrane during operation, which reduces the likelihood of crack formation on the membrane stack as well as on the sensing material, thus improving the lifetime of the device. The sensors' features presented and discussed in this manuscript enable new applications for SMO gas sensors, such as for electronic nose systems and wearable devices used for air and food quality monitoring. Both sensors can be fabricated using conventional MEMS technology, making them more efficient and cost-effective in a long-term perspective. For electrical contact measurement of the sensitive layer resistance and driving heater as well as data processing, the sensors are stacked and subsequently connected to the ASIC with the aid of glue and bonding wires, respectively.

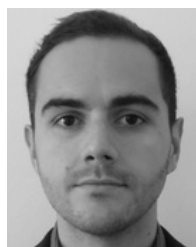
REFERENCES

- [1] K. Kalantar-Zadeh *et al.*, "Intestinal gas capsules: A proof-of-concept demonstration," *Gastroenterology*, vol. 150, no. 1, pp. 37–39, 2016.
- [2] E. Abad *et al.*, "Flexible tag microlab development: Gas sensors integration in RFID flexible tags for food logistic," *Sens. Actuators B, Chem.*, vol. 127, no. 1, pp. 2–7, 2007.
- [3] World Health Organization. (2014). *7 Million Premature Deaths Annually Linked to Air Pollution*. [Online]. Available: www.who.int/mediacentre/news/releases/2014/air-pollution/en/
- [4] FIGARO Inc., Arlington Heights, IL, USA. *TGS 8100—For the Detection of Air Contaminants*. Accessed: Nov. 18, 2017. [Online]. Available: <http://www.figarosensor.com/products/entry/tgs8100.html>
- [5] AMS AG, Unterpremstätten, Austria. *CCS801—Ultra-Low Power Analog VOC Sensor for Indoor Air Quality Monitoring*. Accessed: Nov. 18, 2017. [Online]. Available: <http://ams.com/eng/Products/Environmental-Sensors/Gas-Sensors>
- [6] Sensirion, Staefa, Switzerland. *SGP30—Sensirion Gas Platform*. Accessed: Nov. 18, 2017. [Online]. Available: <https://www.sensirion.com/en/environmental-sensors/gas-sensors/>
- [7] 2017 Annual Creativity in Electronics Awards Announces Finalists from Leading Companies, Design Teams, and Executives in the Electronics Industry. Accessed: Nov. 2, 2017. [Online]. Available: <http://ubm-tech.mediaroom.com/index.php?s=17177&item=138045>
- [8] N. Barsan and U. Weimar, "Conduction model of metal oxide gas sensors," *J. Electroceram.*, vol. 7, pp. 143–167, Dec. 2001.
- [9] D.-D. Lee and D.-S. Lee, "Environmental gas sensors," *IEEE Sensors J.*, vol. 1, no. 3, pp. 214–224, Oct. 2001.
- [10] J. Zhang, X. Liu, G. Neri, and N. Pinna, "Nanostructured materials for room-temperature gas sensors," *Adv. Mater.*, vol. 28, no. 5, pp. 795–831, 2016.
- [11] M. Magno *et al.*, "Low-power gas sensing using single walled carbon nano tubes in wearable devices," *IEEE Sensors J.*, vol. 16, no. 23, pp. 8329–8337, Dec. 2016.
- [12] P. Menini, "Du capteur de gaz à oxydes métalliques vers les nez électroniques sans fil," Ph.D. dissertation, Dept. Micro Nanotechnol./Microelectron., Paul Sabatier Univ.-Toulouse III, Toulouse, France, 2012.
- [13] M. Ortel, Y. S. Trostyanskaya, and V. Wagner, "Spray pyrolysis of ZnO-TFTs utilizing a perfume atomizer," *Solid-State Electron.*, vol. 86, pp. 22–26, Aug. 2013.
- [14] M. Prasad, V. Sahula, and V. K. Khanna, "Design and fabrication of Sidiaphragm, ZnO piezoelectric film-based MEMS acoustic sensor using SOI wafers," *IEEE Trans. Semicond. Manuf.*, vol. 26, no. 2, pp. 233–241, May 2013.
- [15] G. E. Patil, D. D. Kajale, V. B. Gaikwad, and G. H. Jain, "Spray pyrolysis deposition of nanostructured tin oxide thin films," *ISRN Nanotechnol.*, vol. 2012, Jun. 2012, Art. no. 275872.
- [16] A. Bouaoud *et al.*, "Transparent conducting properties of Ni doped zinc oxide thin films prepared by a facile spray pyrolysis technique using perfume atomizer," *Mater. Chem. Phys.*, vol. 137, no. 3, pp. 843–847, 2013.
- [17] E. Li, Z. Cheng, J. Xu, Q. Pan, W. Yu, and Y. Chu, "Indium oxide with novel morphology: Synthesis and application in C₂H₅OH gas sensing," *Cryst. Growth Des.*, vol. 9, no. 5, pp. 2146–2151, 2009.
- [18] R. A. Rani, A. S. Zoolfakar, J. Z. Ou, M. R. Field, M. Austin, and K. Kalantar-Zadeh, "Nanoporous Nb₂O₅ hydrogen gas sensor," *Sens. Actuators B, Chem.*, vol. 176, pp. 149–156, Jan. 2013.
- [19] Z. Tang, P. C. H. Chan, R. K. Sharma, G. Yan, I.-M. Hsing, and J. K. O. Sin, "Investigation and control of microcracks in tin oxide gas sensing thin-films," *Sens. Actuators B, Chem.*, vol. 79, no. 1, pp. 39–47, 2001.
- [20] R. K. Sharma, P. C. H. Chan, Z. Tang, G. Yan, I.-M. Hsing, and J. K. O. Sin, "Investigation of stability and reliability of tin oxide thin-film for integrated micro-machined gas sensor devices," *Sens. Actuators B, Chem.*, vol. 81, no. 1, pp. 9–16, 2001.
- [21] E. Brunet *et al.*, "Comparison of the gas sensing performance of SnO₂ thin film and SnO₂ nanowire sensors," *Sens. Actuators B, Chem.*, vol. 165, no. 1, pp. 110–118, 2012.
- [22] X. Chen, C. K. Y. Wong, C. A. Yuan, and G. Zhang, "Nanowire-based gas sensors," *Sens. Actuators B, Chem.*, vol. 177, pp. 178–195, Feb. 2013.
- [23] N. M. Shaalan, T. Yamazaki, and T. Kikuta, "NO₂ response enhancement and anomalous behavior of n-type SnO₂ nanowires functionalized by Pd nanodots," *Sens. Actuators B, Chem.*, vol. 166, pp. 671–677, Nov. 2012.
- [24] M. Schüller, T. Sauerwald, and A. Schütze, "A novel approach for detecting HMDSO poisoning of metal oxide gas sensors and improving their stability by temperature cycled operation," *J. Sensor Syst.*, vol. 4, no. 2, p. 305, 2015.
- [25] Motiv Inc., San Francisco, USA. *Motiv Ring*. Accessed: Nov. 21, 2017. [Online]. Available: <https://mymotiv.com/>
- [26] COMSOL Multiphysics, COMSOL AB, Stockholm, Sweden.
- [27] I. Simon, N. Bârsan, M. Bauer, and U. Weimar, "Micromachined metal oxide gas sensors: Opportunities to improve sensor performance," *Sens. Actuators B, Chem.*, vol. 73, no. 1, pp. 1–26, 2001.
- [28] S. Roy and C. K. Sarkar, *MEMS and Nanotechnology for Gas Sensors*. Boca Raton, FL, USA: CRC Press, 2015.
- [29] V. V. Sysoev, M. Frietsch, I. Kiselev, and V. V. Sysoev, "Temperature gradient effect on gas discrimination power of a metal-oxide thin-film sensor microarray," *Sensors*, vol. 4, no. 4, pp. 37–46, 2004.
- [30] S. Banerjee, A. Dan, and D. Chakravorty, "Review synthesis of conducting nanowires," *J. Mater. Sci.*, vol. 37, no. 20, pp. 4261–4271, 2002.
- [31] Y. Cui, Q. Wei, H. Park, and C. M. Lieber, "Nanowire nanosensors for highly sensitive and selective detection of biological and chemical species," *Science*, vol. 293, no. 5533, pp. 1289–1292, Aug. 2001.
- [32] N. Yamazoe and N. Miura, "Some basic aspects of semiconductor gas sensors," *Chem. Sensor Technol.*, vol. 4, pp. 19–42, 1992.
- [33] I. Elmi, S. Zampolli, E. Cozzani, F. Mancarella, and G. C. Cardinali, "Development of ultra-low-power consumption MOX sensors with ppb-level VOC detection capabilities for emerging applications," *Sens. Actuators B, Chem.*, vol. 135, no. 1, pp. 342–351, 2008.
- [34] N. H. Kim, D. M. Na, P. J. Ko, J. S. Park, and W. S. Lee, "Electrical and thermal properties of platinum thin films prepared by DC magnetron sputtering for micro-heater of microsensor applications after CMP process," *Solid State Phenomena*, vols. 124–126, pp. 267–270, Jun. 2007.
- [35] H. D. Baehr and K. Stephan, *Wärme- und Stoffübertragung*, 3rd ed. Berlin, Germany: Springer, 1998.
- [36] S. K. H. Fung, Z. Tang, P. C. H. Chan, J. K. O. Sin, and P. W. Cheung, "Thermal analysis and design of a micro-hotplate for integrated gas-sensor applications," *Sens. Actuators A, Phys.*, vol. 54, nos. 1–3, pp. 482–487, 1996.
- [37] M. N. Özışık, *Boundary Value Problems of Heat Conduction*. North Chelmsford, MA, USA: Courier Corporation, 2013.
- [38] Linear Technology Corporation, Milpitas, CA, USA. *LTspice*. Accessed: Jun. 1, 2017. [Online]. Available: www.linear.com/solutions/LTspice
- [39] M. Stadtmüller, "Mechanical stress of CVD-dielectrics," *J. Electrochem. Soc.*, vol. 139, no. 12, pp. 3669–3674, 1992.
- [40] S. Sharma and M. Madou, "A new approach to gas sensing with nanotechnology," *Philos. Trans. Roy. Soc. London A, Math. Phys. Sci.*, vol. 370, pp. 2448–2473, Jan. 2012.

- [41] P. Lall, M. Pecht, and E. B. Hakim, *Influence of Temperature on Microelectronics and System Reliability: A Physics of Failure Approach*. Boca Raton, FL, USA: CRC Press, 1997.
- [42] N. Sabaté *et al.*, "Mechanical characterization of thermal flow sensors membranes," *Sens. Actuators A, Phys.*, vol. 125, no. 2, pp. 260–266, 2006.
- [43] C. Rossi, P. Temple-Boyer, and D. Estève, "Realization and performance of thin SiO₂/SiN_x membrane for microheater applications," *Sens. Actuators A, Phys.*, vol. 64, no. 3, pp. 241–245, 1998.



Ayoub Lahlalia received the M.Sc. degree in microsensors and detection systems from Aix-Marseille University, Marseille, France, in 2016. He is currently pursuing the Ph.D. degree with the Institute for Microelectronics, TU Wien. His scientific interest focuses on gas sensors simulation, characterization, and data processing.



Lado Filipovic received the degree in electrical engineering, the bachelor's degree in engineering in 2006, and the master's degree in applied sciences in 2009 from Carleton University, Ottawa, ON, Canada, and the Ph.D. degree in technical sciences from the Institute for Microelectronics, TU Wien, in 2012, under the supervision of Prof. S. Selberherr. The main focus of his research is the design and simulation of environmental sensors and using metal oxide semiconductors for the detection of toxic gases.



Siegfried Selberherr was born in Klosterneuburg, Austria, in 1955. He received the Dipl.-Ing degree in electrical engineering and the Ph.D. degree in technical sciences from the Technische Universität Wien, in 1978 and 1981, respectively, and the Venia Docendi degree in computer-aided design in 1984. From 1988 to 1999, he was the Head of the Institute for Microelectronics. From 1998 to 2005, he served as the Dean of the Faculty of Electrical Engineering and Information Technology. His current research topics are modeling and simulation of problems for microelectronics engineering.